

An On-Line Fault Diagnosis Method for Power Electronic Drives

Jason M. Anderson, Robert W. Cox, and Jukkrit Noppakunkajorn

Department of Electrical and Computer Engineering

UNC Charlotte

Charlotte, NC 28223

Email: jmander1@uncc.edu, Robert.Cox3@uncc.edu,

Abstract—This paper describes online techniques for monitoring the health of the two most sensitive components in power electronic systems, namely electrolytic filtering capacitors and controllable semiconductor switches (i.e. MOSFETs and IGBTs). The paper begins with a brief discussion of the primary failure mechanisms for these two types of components. It then presents an online technique designed to measure capacitor ESR, which is a key indicator of capacitor health. Subsequent sections address similar online approaches for tracking the on-state resistance of MOSFETs and the collector-to-emitter saturation voltage of IGBTs. Experimental results demonstrate the effectiveness of these techniques.

I. INTRODUCTION

Over the past twenty years, the U.S. Navy has become increasingly interested in electric power technology, including power electronic motor drives [1], [2]. The most poignant example is the move toward the integrated power system (IPS), with its dependence on electric motors and drives for propulsion. The recent effort by the Secretary of the Navy to reduce the fleet's consumption of petroleum-based fuels has led to an even greater push for power electronics as a means to improve efficiency. The potential for savings from variable-speed drives (VSDs), for instance, is tremendous. A 2001 study conducted aboard the *USS Princeton* (CG-59) found that electricity use could be reduced by 20 to 50%, with most of the reduction coming from the adoption of VSDs for motors, pumps, fans, and chillers [3].

The increasing dependence on power electronics, particularly in mission-critical applications, has created a clear need for real-time techniques that detect incipient faults. The two components most prone to failure in switch-mode drives are electrolytic filtering capacitors and controllable power semiconductors (i.e. MOSFETs and IGBTs) [4]. Previous work, particularly with respect to semiconductors, has focused primarily on fault tolerance [5]. For mission-critical applications such as propulsion, this may not be sufficient as failures in fault-tolerant drives can still cause collateral damage [6].

This paper focuses on the detection of incipient faults in digitally-controlled drives. It begins by addressing basic failure mechanisms in electrolytic capacitors and power semiconductors. It then presents on-line techniques for monitoring the health of these components. All of the approaches are predicated on the notion that existing signals arising from the inherent operation of the drive can be used to measure key

indicators of component health. The first proposed method uses a frequency-domain approach to measure capacitor ESR , and the latter two employ a time-domain analysis to measure the on-state resistance of MOSFETs and the collector-to-emitter saturation voltage of IGBTs. Experimental results are presented for each method, and information about future work is presented.

II. FAILURE MECHANISMS IN POWER ELECTRONIC DRIVES

A. Electrolytic Capacitor Failures

Electrolytic bus capacitors are the weakest link in motor drives [4]. Degradation occurs for various reasons, including thermal stresses, transients, reverse bias, and strong vibrations [7]. Thermal stress caused by high ambient temperatures and self-heating from ripple currents is the leading cause of premature failure. This thermal degradation can be neatly summarized. As a capacitor ages, heat from the environment and internal resistance causes the electrolyte to vaporize and escape through the end seal. This loss of electrolyte causes a corresponding increase in ESR . The relationship between these two quantities can be expressed empirically as [8]

$$\frac{ESR}{ESR_0} = \left(\frac{V_0}{V} \right)^2, \quad (1)$$

where ESR and ESR_0 are the corresponding resistance values at time t and time zero; similarly, V and V_0 represent the volume of electrolyte at the same two instants. As V decreases over time, Eq. 1 shows that there is a corresponding increase in ESR . This higher resistance ultimately increases the rate of heat generation, which in turn increases the rate of vaporization. The lower volume of electrolyte then further increases ESR , which in turn increases heating. Ultimately, this positive feedback mechanism accelerates capacitor failure [8]. Because of its central role in the failure process, ESR is a reliable indicator of capacitor health [7], [8].

B. Power Semiconductor Failures

Premature MOSFET failures are caused by a number of different phenomena. The two leading causes are thermal stress and gate oxide breakdown [9]. Both of these mechanisms increase the on-state resistance, $R_{DS,ON}$ [9]. In the case of thermal stress, for instance, dissimilar thermal expansion in the

copper substrate and silicon die cause wear that leads to higher junction temperatures and thus reductions in the mobility and threshold voltage [10], [11]. These changes increase $R_{DS,ON}$, and thus lead to greater heating and ultimately premature failure. The $R_{DS,ON}$ of the MOSFET gradually increases until a sudden drop at the onset of failure [12].

The leading causes of IGBT failures are similar to those noted above for MOSFETs. In IGBTs, thermal stress leads to bond-wire failures and higher junction temperatures. As a result, the collector-to-emitter saturation voltage, $V_{CE,SAT}$, rises [13]. This increase in $V_{CE,SAT}$ indicates an impending failure in the IGBT.

Although drives with appropriate redundancy and fault tolerance can handle complete failures of MOSFETs and IGBTs, it is still important to detect such conditions early. In the case of an IGBT that has experienced significant thermal stress, for instance, the device will short circuit and the bond wires will eventually burn away [6]. This leads to an indeterminate failure state that may cause an arc flash and subsequent collateral damage [13].

Methods proposed for the early detection of this slow degradation are primarily focused on efficiency monitoring [14]. These methods are predicated on the notion that failing components generally have increasing loss mechanisms such as higher IGBT saturation voltages and higher MOSFET on-state resistances [13], [9]. Efficiency monitoring is of limited use in multi-transistor drives, however, because it does not determine the faulty device.

III. FAILURE DETECTION MECHANISM IN ELECTROLYTIC CAPACITORS

A. Method

An on-line impedance spectroscopy technique has been developed to monitor the value of capacitor ESR in a variable-speed AC drive of the form shown in Fig. 1. The block diagram includes a comprehensive low-frequency capacitor model developed from first principles [8], [15], [16]. C_1 is the rated terminal capacitance, R_1 is the resistance of the electrolyte, C_2 is the dielectric capacitance, R_2 is the dielectric loss resistance, and R_0 is the resistance of the foil, tabs, and terminals. This model has been developed specifically for investigation of capacitor performance over the frequency range relevant for DC bus capacitors (i.e. from DC to tens of kiloHertz) [8], [15]. The capacitor current i_C and the AC component \hat{v}_c of the capacitor voltage are monitored.

Figure 2 outlines the proposed online ESR measurement process. Note that the procedure begins with measurements of i_C and \hat{v}_c sampled at several kiloHertz. Figure 3 shows example waveforms. The frequency spectra of these quantities are then computed using the Fast Fourier Transform (FFT). Note that the signals are first modulated with a Hanning window in order to minimize spectral leakage. Figure 4 presents the spectra corresponding to the waveforms of Fig. 3. ESR is ultimately computed by extracting the spectral lines closest to twice the AC line frequency (i.e. 120Hz). In terms

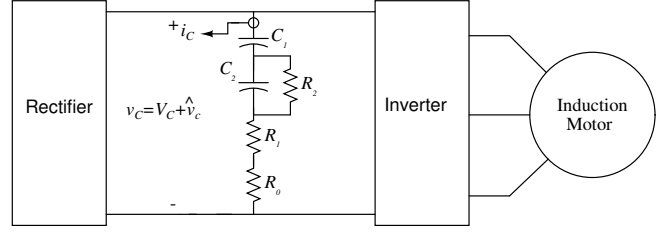


Fig. 1. Block diagram of a typical VSD showing a comprehensive bus capacitor model. The capacitor current, i_C , and AC capacitor voltage, \hat{v}_c , are both measured.

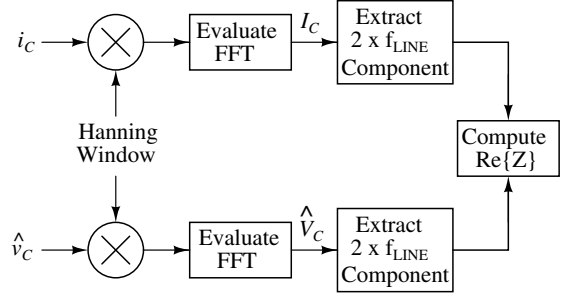


Fig. 2. Block diagram showing the computation of the DC bus capacitor ESR .

of the FFTs defined in Fig. 2, ESR is thus

$$ESR = \Re \left\{ \frac{\hat{V}_C(2f_{line})}{I_C(2f_{line})} \right\}. \quad (2)$$

Measurements are performed at twice the line frequency because physical arguments justify the existence of appreciable signals at that frequency [17]. Content at twice the line frequency results from imbalances between the voltages applied at the input of the six-pulse rectifier. Note that measurements could be performed at any number of other frequencies at which appreciable signal content is expected, such as $6f_{line}$ [17]. It is desirable, however, to avoid frequency content that depends directly on motor speed. In terms of the

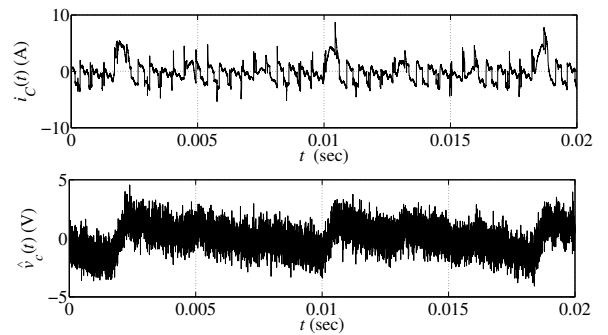


Fig. 3. Measured capacitor current, i_C , and AC capacitor voltage, \hat{v}_c .

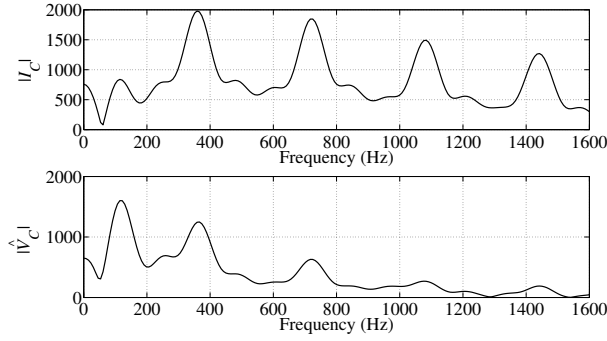


Fig. 4. Magnitudes of the FFTs of the measured capacitor current (top) and the measured AC capacitor voltage (bottom).

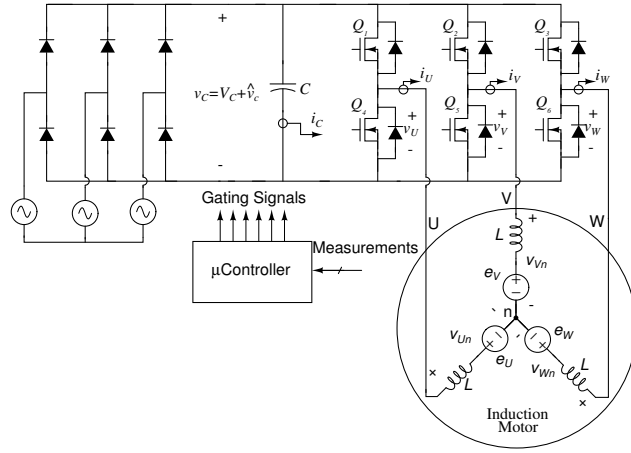


Fig. 5. Partial schematic of the test circuit. A high common-mode amplifier measures the DC bus voltage v_C and a Hall-effect transducer measures i_C . The drain-to-source voltage, v_{DS} , is measured for each MOSFET and the motor phase currents i_U , i_V , and i_W are also measured.

comprehensive capacitor model, Eq. 2 yields

$$ESR = \Re\{Z_{cap}\} = R_1 + R_0 + \frac{R_2}{(1 + \omega^2 R_2^2 C_2^2)}. \quad (3)$$

B. Results

The approach shown in Fig. 2 was used to determine the ESR of a DC bus capacitor in a prototype drive of the form shown in Fig. 5. Accelerated age testing was performed on the prototype using a controlled temperature chamber. The capacitor ESR was found to increase over time as expected [7], [8], [15]. Table I shows the impedance of the DC bus capacitor before and after the accelerated age testing. The capacitor was aged by holding it at its rated temperature for 30 hours. The change in the real part of the capacitor impedance is quite noticeable. Note the results were validated using a BK Precision 889B LCR/ESR Meter.

IV. FAILURE DETECTION MECHANISM IN MOSFETs

A. Method

MOSFET on-state resistance can be measured online in motor drives using naturally-occurring ripple waveforms gen-

TABLE I
MEASURED IMPEDANCE OF DC BUS CAPACITOR BEFORE AND AFTER
ACCELERATED AGING

	Before Aging		After Aging	
	Measured Using Proposed Method	Measured Using LCR/ESR Meter	Measured Using Proposed Method	Measured Using LCR/ESR Meter
$ Z $ (Ω)	1.91	1.9	1.82	1.83
$\angle Z$ ($^\circ$)	-87.29	-87.33	-82.83	-82.08
$\Re\{Z\}$ (Ω)	0.09	0.089	0.226	0.251
$\Im\{Z\}$ (Ω)	-1.91	-1.9	-1.8	-1.81

erated by the action of carrier-based PWM. The relatively short conduction time of the MOSFETs in a PWM drive makes it difficult to use a frequency-domain approach as described for the measurement of capacitor ESR . On-state resistance is better measured using a time-domain approach. The exact details depend upon the manner in which the drive is controlled.

Consider the motor drive shown in Fig. 5, and assume that it is driven using a digitally-implemented carrier-based PWM scheme. Specific instances of carrier-based PWM include space-vector modulation and regular sampling [18]. Typically, these schemes are implemented using capture-compare modules in microcontrollers. The most common technique is to use timers to align the switching instants with a fictitious carrier waveform as shown in Fig. 6. As a result, each phase voltage pulses once per switching period. The exact timing of switching depends upon the specifics of the microcontroller, but switching is often selected to be symmetrically aligned with the peaks of the carrier as shown in Fig. 6 [18]. The measurement approach described below does not depend on this symmetry, however. Symmetric regular sampling is used only for illustrative purposes, and other techniques could be considered.

The proposed measurement approach is based on the current ripple generated by the phase voltages shown in Fig. 6. These voltage waveforms can be written as the superposition of a fundamental frequency component and a ripple term. Using the simplified induction machine equivalent circuit in Fig. 5, note that all of the voltage ripple for a given phase appears across the inductance L . The resulting current is thus of the form [17]

$$i_{ripple} = \frac{1}{L} \int_0^t v_{ripple}(\tau) d\tau. \quad (4)$$

The term v_{ripple} can be written for any one of the three phases. For phase U, for instance, it is

$$v_{U,ripple} = v_{Un} - v_{Un,1} \quad (5)$$

where v_{Un} is the voltage across phase U with respect to the motor neutral and $v_{Un,1}$ is the corresponding fundamental component of v_{Un} . In terms of the phase voltages shown in Fig. 6 [17],

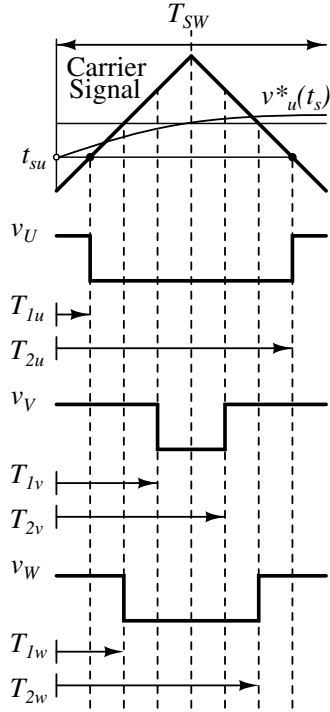


Fig. 6. Notional example of the voltages v_U , v_V , and v_W during a single switching period. Also shown is the fictitious triangular carrier signal and the reference waveform for phase U. The voltages are defined in Fig. 5. The switching time instants, T_1 and T_2 , are also shown for each of the phases.

$$v_{Un} = \frac{2}{3}v_U - \frac{1}{3}(v_V + v_W). \quad (6)$$

A careful analysis of Eqs. 4, 5, and 6 shows that the pulses in v_V and v_W affect the ripple current flowing in phase U. If one measures the voltage across Q_4 during an appropriate interval aligned with one of the pulses on the other two phase legs, then one can easily estimate the on-state resistance of Q_4 using the equation

$$R_{DS,4,ON} = \frac{\Delta v_U}{\Delta i_U}, \quad (7)$$

where Δi_U is the ripple current during the measurement interval and Δv_U is the corresponding voltage ripple. Figure 7 presents an experimental example showing how the ripple current changes as the MOSFETs change state. $R_{DS,4,ON}$ would be measured when v_V is low. The on-state resistance of the other FETs would be measured during similar intervals.

Timing is critical to the successful implementation of the measurement process described above. Figure 6, for instance, shows times during which Q_4 , Q_5 , and Q_6 are each conducting. Note that Q_4 is on for the longest time, and that its ripple current should exhibit 5 distinct states based on the action of the other phase legs. By comparison, the ripple current flowing through Q_5 only exhibits one distinct state. In this case, one can trigger high-speed sampling of the voltage and current for Q_4 using the same interrupts that control the

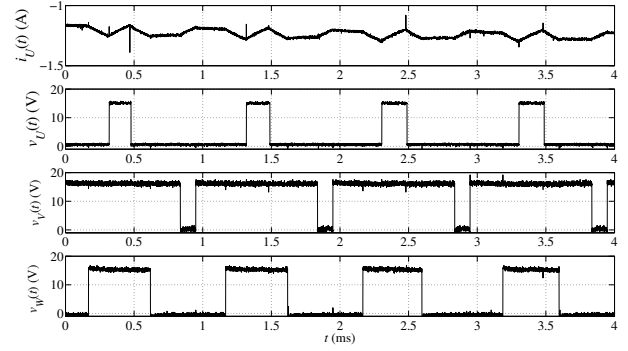


Fig. 7. The nature of i_U , v_U , v_V , and v_W (from top to bottom) in the example drive.

switching of Q_5 . Thus, one can exploit the nature of the PWM waveforms to obtain the best possible measurements of Δi and Δv . Measurements should be performed over a sufficiently long interval during which the current is approximately linear. The timing shown in Fig. 6, for instance, is ideal for the measurement of $R_{DS,4,ON}$ because the pulses on the two other phases are of a sufficient length and do not overlap. One can predetermine the appropriate measurement times by considering the nature of the symmetric, center-aligned PWM signals shown in Fig. 6. For any one phase, the switching time instants T_1 and T_2 can be computed in real time using the geometrical relationships [18]

$$T_1 = \frac{1}{4}T_{SW} \cdot (1 + v^*(t_s)) \quad (8)$$

$$T_2 = \frac{1}{2}T_{SW} + \frac{1}{4}T_{SW} \cdot (1 - v^*(t_s)) \quad (9)$$

where $v^*(t_s)$ is the most recent sample of the reference waveform for the given phase. When using regular sampling, these references are of the form

$$v_u^*(t_s) = M \sin(\omega_m t_s) \quad (10)$$

$$v_v^*(t_s) = M \sin\left(\omega_m t_s - \frac{2\pi}{3}\right) \quad (11)$$

$$v_w^*(t_s) = M \sin\left(\omega_m t_s + \frac{2\pi}{3}\right) \quad (12)$$

where M is the modulation depth and ω_m is the angular frequency of the modulating signal. The pulse widths for each phase are thus computed by taking the difference

$$\Delta T = T_2 - T_1 = \frac{1}{2}T_{SW} - \frac{1}{2}T_{SW} \cdot (v^*(t_s)). \quad (13)$$

These times are independent of ω_m and can thus be rewritten by substituting $\omega_m t_s = \theta$ into (10)-(13) to yield

$$\Delta T_u = \frac{1}{2}T_{SW} - \frac{1}{2}T_{SW} \cdot M \sin(\theta) \quad (14)$$

$$\Delta T_v = \frac{1}{2}T_{SW} - \frac{1}{2}T_{SW} \cdot M \sin\left(\theta - \frac{2\pi}{3}\right) \quad (15)$$

$$\Delta T_w = \frac{1}{2}T_{SW} - \frac{1}{2}T_{SW} \cdot M \sin\left(\theta + \frac{2\pi}{3}\right). \quad (16)$$

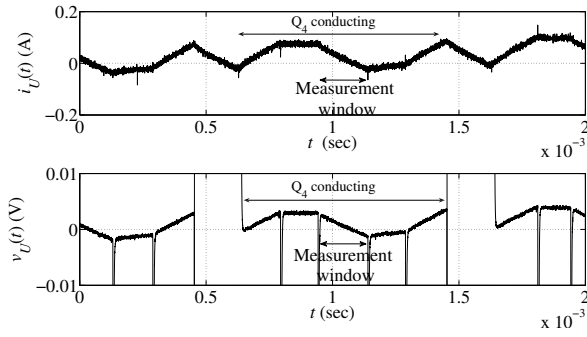


Fig. 8. Measured $i_U(t)$ and $v_U(t)$. The measurement window is indicated.

Equations (14)-(16) can be plotted to determine appropriate measurement times. Figure 6 corresponds to $M = 1$ and $\theta = -2\pi/3$. One can perform analysis to determine if the current will be approximately linear during the chosen measurement period. The measurement timing can be easily coordinated with switching.

B. Results

The proposed measurement scheme has been demonstrated using a prototype drive of the form shown in Fig. 5. In this case, the motor is a 1hp induction machine, the microcontroller is a dsPIC30F6010A, and the MOSFETs are IRF540s. The microcontroller generates center-aligned PWM waveforms. Figure 8 shows the drain-to-source voltage across Q_4 and the phase U current. Δi_U and Δv_U are measured over the indicated window. As described above, the measurement is relatively straightforward to implement because the appropriate sampling window can be predetermined. Measurements are performed once every 100 periods of the modulating waveform. When applying the proposed approach with the waveforms shown in Fig. 8, the value of $R_{DS,ON}$ was found to be 40.2m Ω . For the given conditions (i.e. ambient temperature and current), the manufacturer datasheet predicts a value of 44m Ω [19].

To test the detection mechanism, the drive was placed into a temperature controlled chamber. A thermocouple was connected to the case of MOSFET Q_4 to record the temperature during testing. $R_{DS,ON}$ was calculated while the drive was heated from a case temperature of 45°C to 105°C as seen in Fig. 9. The value of $R_{DS,ON}$ was computed using the method described above and it was found to vary from 46.2m Ω at a case temperature of 45°C to 71.6m Ω at a case temperature of 105°C. Note that a full-scale diagnostic indicator would require one to determine if $R_{DS,ON}$ has changed because of actual faults or simply because of other natural phenomena such as changes in ambient temperature. Work in this area is ongoing.

V. FAILURE DETECTION MECHANISM IN IGBTs

A. Method

A similar time-domain approach can be used determine the health of an IGBT. In this case, one measures the collector-to-

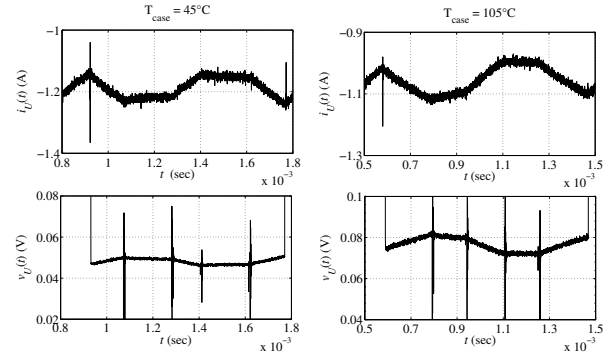


Fig. 9. Measured $i_U(t)$ and $v_U(t)$ at 45°C (left) and at 105°C (right).

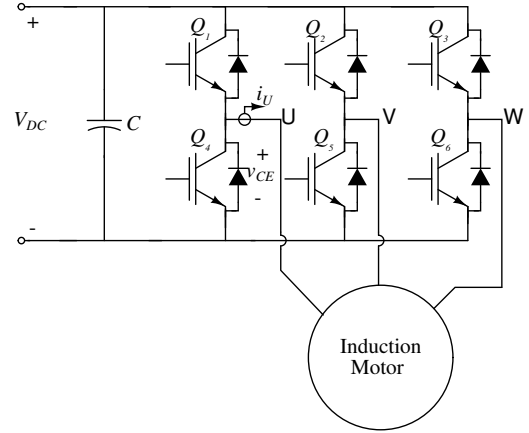


Fig. 10. Schematic of the laboratory prototype with IGBTs replacing the MOSFETs. Voltages are actually measured across all six IGBTs.

emitter saturation voltage ($V_{CE,SAT}$). $V_{CE,SAT}$ is recognized as an indicator of bond-wire degradation, a failure mechanism that slowly arises as the device is exposed to various thermal cycles over its lifetime [13]. Again, this value can be measured if one exploits the nature of the PWM waveforms used in the drive. In this case, one measures the collector-to-emitter voltage and phase current when the IGBT is conducting for a sufficiently long period. Again, sampling is easily triggered because the switching signals can be pre-calculated for a given modulating frequency. Measurements are performed during a pre-selected switching period once every 100 cycles of the modulating waveform. If the load on the motor changes, the resulting phase shift in the current may cause the IGBT's parallel diode to conduct during part of the measurement window. Since this is not acceptable, the measurement window must be shifted to an adjacent switching cycle; this is easily accommodated.

B. Results

Figure 11 shows experimental results for one of the low-side IGBTs in a six-switch, three-phase drive of the form shown in Fig. 10. The measured value of $V_{CE,SAT}$ is found to be approximately 0.7V by averaging over the indicated

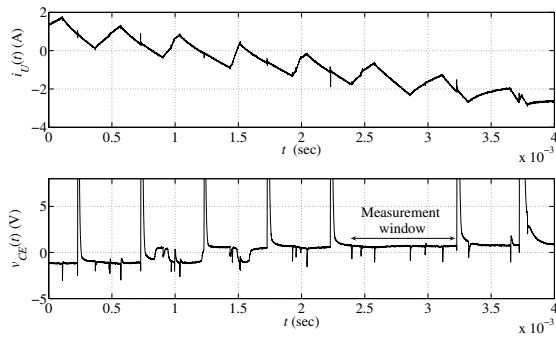


Fig. 11. Top: Current in phase U of the laboratory prototype. Bottom: v_{CE} across the bottom IGBT in the U-phase leg of the laboratory inverter.

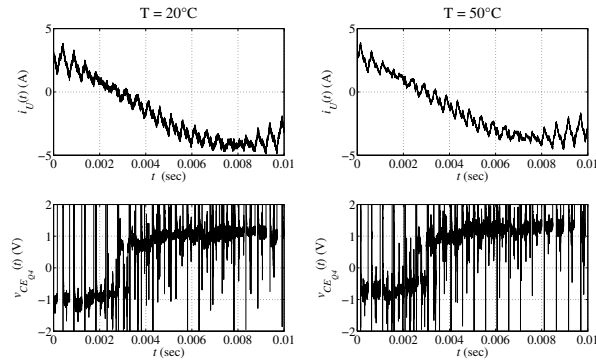


Fig. 12. Measured $i_U(t)$ and $v_{CE}(t)$ for Q_4 in Fig. 10 at 20°C (left) and 50°C (right).

window. This value matches closely to the manufacturer's data (0.75V) for the given current, ambient temperature, and gate voltage [20].

To test the detection mechanism, the drive was placed into a temperature controlled chamber. A thermocouple was connected to the case of the IGBT module to record the temperature during testing. The voltage $V_{CE,SAT}$ across the bottom IGBT of phase U (Q_4) was measured while the drive was heated from a case temperature of 20°C to 50°C. Figure 12 shows results at the starting and ending conditions. $V_{CE,SAT}$ was computed using the method described above. It was found to be .72V at a case temperature of 20°C, and .92V at a case temperature of 50°C. Again, this result is consistent with the literature, but future work is still needed in order to develop a comprehensive diagnostic indicator.

VI. CONCLUSION

Online methods for the detection of incipient faults will be essential as the fleet becomes more heavily dependent on power electronics. This paper has demonstrated techniques for measuring key health indicators in these systems. Additional future work is needed to develop complete diagnostic and prognostic activities.

REFERENCES

- [1] N. H. Doerry, "Institutionalizing the electric warship," *Naval Engineers Journal*, vol. 118, no. 4, pp. 57–64, 2006.
- [2] —, "NGIPS technology development roadmap," NAVSEA, Tech. Rep., Nov 2007.
- [3] C. Lotspeich and A. Lovins, "Energy efficiency survey aboard USS Princeton CG-59," Rocky Mountain Institute, Tech. Rep., 2001.
- [4] Military Handbook 217 F, *Reliability prediction of electronic equipment, revision F*, Notice 1, 10 July 1992, Notice 2, Feb. 28, 1995, ed., Dec. 1991.
- [5] D. Kastha and B. K. Bose, "Investigation of fault modes of voltage-fed inverter system for induction motor drive," *IEEE Trans. Ind. Appl.*, vol. 30, p. 10281038, Jul/Aug 1994.
- [6] N. D. Benavides, T. J. McCoy, and M. A. Chrin, "Reliability improvements in integrated power systems with pressure-contact semiconductors," in *Proc. ASNE Day*, Apr 2009.
- [7] C. Kulkarni, G. Biswas, and X. Koutsoukos, "A prognosis case study for electrolytic capacitor degradation in DC/DC converters," in *Proc. Annual Conf. of the Prognostics and Health Management Society 2009*, San Diego, Oct 2009.
- [8] M. L. Gasperi, "Life prediction modeling of bus capacitors in ac variable-frequency drives," *IEEE Trans. Ind. Appl.*, vol. 41, no. 6, pp. 1430–1435, Nov./Dec. 2005.
- [9] R. Orsagh, D. Brown, M. Roemer, T. Dabnev, and A. Hess, "Prognostic health management for avionics system power supplies," in *Proc. 2005 IEEE Aerospace Conf.*, Mar. 2005, pp. 3585 – 3591.
- [10] J. Celaya, A. Saxena, P. Wysocki, S. Saha, and K. Goebel, "Towards prognostics of power MOSFETs: Accelerated aging and precursors of failure," in *Proc of Annual Conference of the Prognostics and Health Management Society*, Portland, Oregon, Oct. 2010.
- [11] B. Baliga, *Fundamentals of Power Semiconductor Devices*. New York, NY: Springer LLC, 2008.
- [12] J. Celaya, N. Patil, S. Saha, P. Wysocki3, and K. Goebel, "Towards accelerated aging methodologies and health management of power MOSFETs (technical brief)," in *Proc. of Annual Conference of the Prognostics and Health Management Society*, San Diego, CA, Sept./Oct. 2009.
- [13] M. Ciappa and W. Fichtner, "Lifetime prediction of IGBT modules for traction applications," in *Proc. IEEE Reliability Physics Symposium*, San Jose CA, 2000, pp. 210–216.
- [14] J. Morroni, A. Dolgov, R. Zane, and D. Maksimovi, "Online health monitoring in digitally controlled power converters," in *Proc. IEEE Power Electron. Specialists Conf.*, Orlando, FL, Jun 2007.
- [15] M. Gasperi, N. Gollhardt, and R. Sladky, "A model for equivalent series resistance in aluminum electrolytic capacitors," in *Proc. Capacitor and Resistor Technology Symp. (CARTS)*, Jupiter, FL, Mar. 1997, pp. 71–75.
- [16] J. Scholte and W. C. van Geel, "Impedances of the electrolytic rectifier," Philips Res. Rep, Tech. Rep., 1953.
- [17] N. Mohan, T. Undeland, and W. Robbins, *Power Electronics Converters, Applications, and Design*, T. Edition, Ed. John Wiley & Sons, 2003.
- [18] J. Holtz, "Pulsewidth modulation for electronic power conversion," *Proc. IEEE*, vol. 82, no. 8, pp. 1194–1214, Aug 1994.
- [19] "IRF540N HEXFET power MOSFET," International Rectifier, Tech. Rep., 2001.
- [20] "Toshiba intelligent power module MIG20J503H," Toshiba, Tech. Rep., 2003.